# Transition from metal to semiconductor by semi-hydrogenation of borophene

Mohammad Ali Mohebpour,[1] Shobair Mohammadi Mozvashi,[1] Sahar Izadi Vishkayi,[2] and Meysam Bagheri Tagani[1,*]

[1]*Computational Nanophysics Laboratory (CNL), Department of Physics, University of Guilan, P. O. Box 41335-1914, Rasht, Iran*

[2]*School of Physics, Institute for Research in Fundamental Sciences (IPM), P. O. Box 19395-5531, Tehran, Iran*

(Received 21 September 2021; revised 23 December 2021; accepted 19 January 2022; published 31 January 2022)

Borophene has triggered a surge of interest due to its outstanding properties including mechanical flexibility, polymorphism, and optoelectrical anisotropy. Very recently, a novel semi-hydrogenated borophene, called $\alpha'$-4H, was synthesized in large-scale freestanding samples, exhibiting excellent air-stability and semiconducting nature. Herein, using the density functional theory (DFT) and many-body perturbation theory (MBPT), we investigate the electronic and excitonic optical properties of $\alpha'$-4H borophene. The DFT results reveal that hydrogenation breaks the mirror symmetry and increases the buckling height of pure $\alpha'$ borophene, which results in an orbital hybridization and indirect band gap of 1.49 eV in $\alpha'$-4H borophene. Moreover, the optical spectrum achieved from solving the Bethe-Salpeter equation (i.e., GW+BSE) shows an optical band gap of 2.40 eV, which corresponds to a strongly bound and stable bright exciton with a binding energy of 1.18 eV. The mean value of absorption within the visible area is 1.68 $(1.13)\times10^7$ $m^{-1}$ for $E\|x$ $(E\|y)$ polarization, which shows a linear dichroism for visible light. The effective mass and Bohr radius of the ground-state exciton are 0.78 $m_0$ and 2.03 Å, respectively, which demonstrates the characteristics of Frenkel exciton. The excitonic states are robust against tension up to 10%, under which the monolayer is dynamically stable. We also study the bilayer $\alpha'$-4H borophene with different stackings. For the weak van der Waals interactions between the layers, the bilayer preserves most of the structural and electronic properties of the monolayer. Our study exposes the underlying physics behind the structural, electronic, and optical properties of $\alpha'$-4H borophene and suggests it as a very promising candidate for flexible optoelectronic applications.

DOI: 10.1103/PhysRevMaterials.6.014012

## I. INTRODUCTION

Two-dimensional (2D) boron, known as borophene, is recently considered as a game-changing player of future electronics because of its exceptional properties including polymorphism, electronic and optical anisotropy, ultrahigh thermal conductance, optical transparency, and phonon-mediated superconductivity [1–5]. Moreover, short B-B bonds and low atomic mass leads to very outstanding mechanical characteristics in borophene [6,7]. Numerous works have studied the applications of borophene in rechargeable ion batteries, gas storages, catalysts, and sensors [8–11]. Moreover, borophene has been recently focused on for its potentials in flexible electronics, wearable devices, and medicines, owing to its flexible nature, low mass density, and nontoxicity [12,13].

Boron has three valence electrons. To compensate the octet completion deficiency, it tends to make highly-delocalized multicenter bonds, resulting in a vast structural diversity and polymorphism [14]. Up to now, several phases of borophene have been proposed and synthesized, including $\alpha$, $\alpha'$, $\beta$, and $\chi$ phases, which have trigonal structures with different numbers and positions of hexagon holes (HHs) [15,16]. The different phases of borophene are defined in terms of parameter $\nu = n/N$, where $n$ and $N$ are the numbers of HHs of the phase and boron atoms in a pristine triangular unit cell, respectively. The physical properties of borophene strongly depend on this morphology variable, therefore, there is a wide set of options to synthesize a borophene sheet with desired properties.

Due to its atomic arrangement, borophene cannot be exfoliated mechanically. Therefore, other methods such as chemical vapor deposition, molecular beam epitaxy, and liquid phase exfoliation should be used [17]. Moreover, because of its electron deficiency, borophene cannot be stable in a free-standing form and requires the support of a metal substrate [18,19]. To date, several successful syntheses of borophene have been reported on Ag, Cu, Ni, and Au substrates [20–22]. The Ag, Cu, and Ni substrates donate electrons to, and Au substrate withdraws electrons from borophene, hence, the borophene grow flat on the former substrates and buckled on the latter one [6,23].

Because of its high reactivity, most of boron nanostructures suffer from rapid oxidation and presence of other ambient contaminations [6]. Surface modification is known as a capable tool for enhancing the stability and reducing the surface reactivity of nanostructures [24–26]. Specifically, hydrogenation is reported widely to have a major impact on the stability of borophene and other two-dimensional materials [27–30].

Recently, Hou *et al.* [12] have prepared a novel semi-hydrogenated borophene phase in large quantities by *in situ* decomposition of $NaBH_4$ under the exposure of hydrogen. This borophene was named $\alpha'$-4H because it is similar to $\alpha'$ borophene [31] with 4 adsorbed hydrogen atoms in each

*m_bagheri@guilan.ac.ir

 

unit cell. The $\alpha'$-4H borophene has three major advantages, which make it very fascinating. First, it has high dynamical stability in freestanding form. By withdrawing electrons from boron atoms, hydrogenation acts similar to a withdrawing substrate, resulting in a stable buckled structure. Second, it is stable in the air condition with long lifetime. The screening of hydrogen passivates the surface of borophene and prevents it from reactions with oxygen or other ambient atoms. And third, unlike other phases, $\alpha'$-4H borophene has an energy band gap of $\sim 2.5$ eV, which brings hopes for its applications as a semiconductor.

Discussing theunderlying physics behind the quantum systems improves the physical insights and enhances the theory for future advances. To contribute to the discussion, in our previous paper, we systematically investigated the mechanical flexibility and strength of $\alpha'$-4H borophene by first-principle calculations [32]. We calculated Young's modulus, ideal strength, and critical strain to be 195.56 N/m, 14.06 N/m, and 16%, respectively. We also demonstrated the dynamical stability, mechanical anisotropy, and tunable band gap for this monolayer.

In this paper, using density functional theory, we initially investigate the microscopic aspects in which the metallic $\alpha'$ borophene turns into the semiconducting $\alpha'$-4H. We show how hydrogenation leads to an orbital hybridization and a wide band gap.

Then, we solve the Bethe-Salpeter equation on top of different levels of the GW (GW+BSE) to obtain the optical spectrum including many-body effects. We find that the direct optical excitation is characterized by an optical band gap of 2.40 eV, which corresponds to a strongly bound and stable exciton with a binding energy of 1.18 eV.

The mean value of absorption within the visible area is calculated to be 1.68 and 1.13 $\times 10^7$ m$^{-1}$ for $E\|x$ and $E\|y$ polarizations, respectively, which shows a linear dichroism for visible light. Importantly, we calculate the effective mass and Bohr radius of the ground-state exciton to be 0.78 $m_0$ and 2.03 Å, respectively, which tell us the excitons in $\alpha'$-4H borophene have the characteristics of Frenkel exciton. We also indicate that the excitonic states are robust against tension up to 10%, under which the monolayer is dynamically and mechanically stable. Finally, we investigate the bilayer $\alpha'$-4H borophene with different stackings. We realize that for the weak van der Waals interaction between the layers, the bilayer preserves most of structural and electronic properties of the monolayer and can be used for similar applications. Our results bring valuable insights about the physical properties of the monolayer and bilayer $\alpha'$-4H borophene and suggest it as a promising material for flexible optoelectronic applications.

## II. THEORETICAL BACKGROUND

We start the density functional theory (DFT) calculation to find the ground-state eigenvalues ($E_{nk}$) and eigenfunctions ($\Phi_{nk}$) by solving the Kohn-Sham equation given below:

$$(T + V_{n-e} + V_H + V_{xc})\Phi_{nk} = E_{nk}\Phi_{nk}, \tag{1}$$

where T is the kinetic energy operator, $V_{n-e}$ the Coulomb potential of the nuclei, $V_H$ the Hartree potential, and $V_{xc}$ the exchange-correlation potential. The quasiparticle (QP) energies ($E_{nk}^{\mathrm{QP}}$) are determined within the GW approximation as a first-order perturbative correction to the DFT single-particle energies ($E_{nk}$) [33,34]:

$$\begin{aligned} E_{nk}^{\mathrm{QP},1} = \mathrm{Re}[\langle\Phi_{nk}|\, T + V_{n-e} + V_H + \Sigma_{xc}(G, W; E_{nk}) \\ |\Phi_{nk}\rangle] = E_{nk} + \langle\Phi_{nk}|\Sigma^{GW} - V_{xc}|\Phi_{nk}\rangle\,, \end{aligned} \tag{2}$$

where $\Sigma = iG_0W_0$ is the self-energy operator. This equation is solved nonself-consistently. Therefore, it is the simplest level of theory (the so-called $G_0W_0$) and computationally the most efficient one. It calculates the QP energies from a single iteration by neglecting all off-diagonal elements of the self-energy and employing a Taylor expansion of the self-energy around the DFT energies. The noninteracting Green's function ($G_0$) is directly calculated from single-particle orbitals and energies as

$$G_0(r, r', \omega) = \sum \frac{\Phi_{nk}(r)\Phi_{nk}^*(r')}{\omega - E_{nk} - i\eta\ \mathrm{sgn}(E_F - E_{nk})}, \tag{3}$$

where $E_F$ is the Fermi energy and $\eta$ a positive infinitesimal quantity. The noninteracting screened Coulomb potential ($W_0$) is obtained by the inverse dielectric function ($\varepsilon^{-1}$) and bare Coulomb interaction ($\upsilon$) as below [35]:

$$W_0(r, r', \omega') = \int dr''\varepsilon^{-1}(r, r'', \omega')\upsilon(r'', r'). \tag{4}$$

At higher levels of theory (i.e., $G_iW_0$ and $G_iW_i$), the updated QP energies ($E_{nk}^{\mathrm{QP},i+1}$) are achieved from the QP energies of the previous iteration as follows:

$$\begin{aligned} E_{nk}^{\mathrm{QP},i+1} = E_{nk}^{\mathrm{QP},i} + Z_{nk}\mathrm{Re}\big[\,\langle\Phi_{nk}|\, T + V_{n-e} \\ + V_H + \Sigma_{xc}(G, W; E_{nk})\,|\Phi_{nk}\rangle - E_{nk}^{\mathrm{QP},i}\big], \end{aligned} \tag{5}$$

where the renormalization factor ($Z_{nk}$) is given by [36–38]

$$Z_{nk} = \left(1 - \mathrm{Re}\,\langle\Phi_{nk}|\,\frac{\partial}{\partial\omega}\Sigma(\omega)_{|_{E_{nk}^{\mathrm{QP},i}}}\,|\Phi_{nk}\rangle\right)^{-1}. \tag{6}$$

At the $G_iW_0$ level, the Green's function ($G$) is iteratively updated while the screened Coulomb potential ($W$) is kept fixed at the initial DFT value. At the $G_iW_i$ level, both of them are reevaluated at each iteration ($i$). Here, the interacting Green's function is linked to its noninteracting version with the Dyson equation given as $G = G_0 + G_0\Sigma G$ [39].

The imaginary part of the macroscopic dielectric function ($\epsilon$) is obtained by summation over the empty conduction bands within the long-wavelength limit ($q \to 0$) [40]:

$$\begin{aligned} \mathrm{Im}\varepsilon_{ij}(\omega) = \frac{4\pi^2e^2}{\Omega}\lim_{q\to 0}\frac{1}{|q|^2}\sum_{c,v,k} 2w_k\delta(\varepsilon_{ck} - \varepsilon_{vk} - \omega) \\ \times\ \langle u_{ck+e_iq}|u_{vk}\rangle\,\langle u_{ck+e_jq}|u_{vk}\rangle^*\,, \end{aligned} \tag{7}$$

where $q$ is the Bloch vector of the incident wave, $w_k$ the $k$-point weight, $\Omega$ the volume of the unit cell, and $u_{ck}$ the periodic part of the wave function. The $e_{i(j)}$ is the unit vector of the three Cartesian directions, which corresponds to light polarization. We investigate linear polarizations, including $E\|x$ ($\varepsilon_{xx}$), $E\|y$ ($\varepsilon_{yy}$), and $E\|z$ ($\varepsilon_{zz}$). The indices $c$ and $v$ correspond to the conduction and valence band states, respectively.

The real part of the dielectric function is transformed by use of the Kramers-Kronig relation:

$$\mathrm{Re}\epsilon_{ij}(\omega) = 1 + \frac{2}{\pi} P \int_0^\infty \frac{\omega' \mathrm{Im}\epsilon_{ij}(\omega)}{\omega'^2 - \omega^2 + i\eta} d\omega' \tag{8}$$

where $P$ is the principle value and $\eta$ the complex shift, which was set to 0.1 to obtain a perfect acceptance in all of our calculations.

The electron-hole excited states are characterized by the expansion [41]:

$$|S\rangle = \sum_c^{\text{elec}} \sum_v^{\text{hole}} \sum_k A^S_{cvk} |cvk\rangle , \tag{9}$$

where $A^S$ is the amplitude of a free electron-hole pair configuration composed of the electron state $|ck\rangle$ and the hole state $|vk\rangle$. It is achieved from the diagonalization of the following excitonic equation [42,43]:

$$\left(E^{\mathrm{QP}}_{ck} - E^{\mathrm{QP}}_{vk}\right) A^S_{cvk} + \sum_{c'v'k'} \langle cvk|\Xi^{e-h}|c'v'k'\rangle A^S_{c'v'k'} = \Omega^s A^s_{cvk}, \tag{10}$$

where $E^{\mathrm{QP}}_{ck}(E^{\mathrm{QP}}_{vk})$ denotes the QP eigenvalues of valence (conduction) band at a specific $k$ point, kernel $\Xi^{e-h}$ describes the screened interaction between excited electrons and holes, and $\Omega^S$ is the excitation energy.

Further optical analyses can be performed using the imaginary and real parts of the dielectric function. Electron energy loss ($L$), refractive index ($n$), and extinction coefficient ($k$) are calculated through:

$$L_{ij} = \frac{\mathrm{Im}\epsilon_{ij}}{\mathrm{Re}\epsilon^2_{ij} + \mathrm{Im}\epsilon^2_{ij}}, \tag{11}$$

$$n_{ij} = \sqrt{\frac{\sqrt{\mathrm{Re}\epsilon^2_{ij} + \mathrm{Im}\epsilon^2_{ij}} + \mathrm{Re}\epsilon_{ij}}{2}}, \tag{12}$$

$$k_{ij} = \sqrt{\frac{\sqrt{\mathrm{Re}\epsilon^2_{ij} + \mathrm{Im}\epsilon^2_{ij}} - \mathrm{Re}\epsilon_{ij}}{2}}. \tag{13}$$

Subsequently, the absorption coefficient ($\alpha$) and reflectance ($R$) are given by

$$\alpha_{ij} = 2\frac{\omega}{c} k_{ij}, \tag{14}$$

$$R_{ij} = \frac{\left(1 - n^2_{ij}\right) + k^2_{ij}}{\left(1 + n^2_{ij}\right) + k^2_{ij}}. \tag{15}$$

The effective mass ($\mu$) and Bohr radius ($a_x$) of the ground-state exciton are calculated based on the hydrogenoid model [44]:

$$\mu = \frac{E_b}{R_h} \times \varepsilon_r^2 \times m_0, \tag{16}$$

$$a_x = \frac{\varepsilon_r}{\mu} \times a_h \times m_0, \tag{17}$$

where $R_h$ is the Rydberg constant (13.6 eV), $\varepsilon_r$ the dielectric constant, $m_0$ the electron rest mass, and $a_h$ the Bohr radius (0.529 Å).

## III. COMPUTATIONAL DETAILS

The first-principles calculations were performed in the framework of DFT, using the Quantum ESPRESSO package [45], the generalized gradient approximation developed by Perdew-Burke-Ernzerhof (GGA-PBE), and the projector augmented waves (PAW) pseudopotentials [40,46]. The energy cutoff was set to be 600 eV. The Brillouin zone was integrated with a 13× 13 × 1 Γ-centered $k$-point mesh. The atomic positions and lattice parameters were fully relaxed until a force convergence of $10^{-3}$ eV/Å was achieved. The convergence threshold for energy minimization was selected to be $10^{-7}$ eV. To avoid spurious interactions between layers, the vacuum space was considered to be $L_z = 20$ Å. To understand the bond characteristics, the charge transfer was determined using the Bader method [47].

The Raman spectrum was calculated from the second order derivative of the electronic density matrix with respect to a uniform electric field, as proposed by Lazzeri *et al.* [48] and implemented in Quantum ESPRESSO package. Moreover, the STM images were calculated through the Tersoff-Hamann method, which is a simple model of an s-wave STM tip [49,50]. More details are available in the Supplemental Material [51], Text S1.

The many-body perturbation calculations were carried out using the GW approximation. The eigenvalues and eigenstates achieved from the DFT-PBE were served as input to calculate the QP energies. The calculations were performed at different levels of self-consistency including single-shot (i.e., $G_0W_0$) and partially self-consistent (i.e., $GW_0$ and GW). A compromised set of input parameters (e.g., 9 × 9 × 1 $k$-point mesh, $L_z = 25$ Å, 40 virtual bands, and 4 iterations) was utilized for the GW calculations. The QP band structure was interpolated at the $G_0W_0$ level using the maximally localized Wannier functions (MLWFs) implemented in the WANNIER90 code [52]. The $sp^3$ and $s$ orbitals of B and H atoms were respectively chosen for the initial projections.

The excitonic optical properties were investigated by solving the Bethe-Salpeter equation (BSE) on top of GW eigenvalues and wave functions, using the Tamm-Dancoff approximation (TDA). This approximation takes only the resonant part of the BS Hamiltonian into account. The 10 highest valence bands and the 10 lowest conduction bands were considered as the basis for the excitonic eigenstates.

## IV. RESULTS AND DISCUSSION

### A. Structural and electronic properties

The structural configurations of fully relaxed $\alpha'$ and $\alpha'$-4H borophenes are displayed in Figs. 1(a) and 1(b) and the corresponding structural parameters are listed in Table S1 of the Supplemental Material [51]. The pure $\alpha'$ borophene is nearly flat ($\Delta = 0.37$ Å) and isotropic, with a hexagon hole concentration of $\nu = 1/9$. The hydrogenation leads to an increase in the buckling in $\alpha'$-4H borophene ($\Delta = 0.88$ Å), owing to the attraction between B and H atoms. The lattice constants of the two monolayers are similar (5.05 Å) but the isotropy of the lattice breaks after hydrogenation. As a result, the bond length increases from isotropic 1.68 Å to anisotropic 1.69 and 1.77 Å.

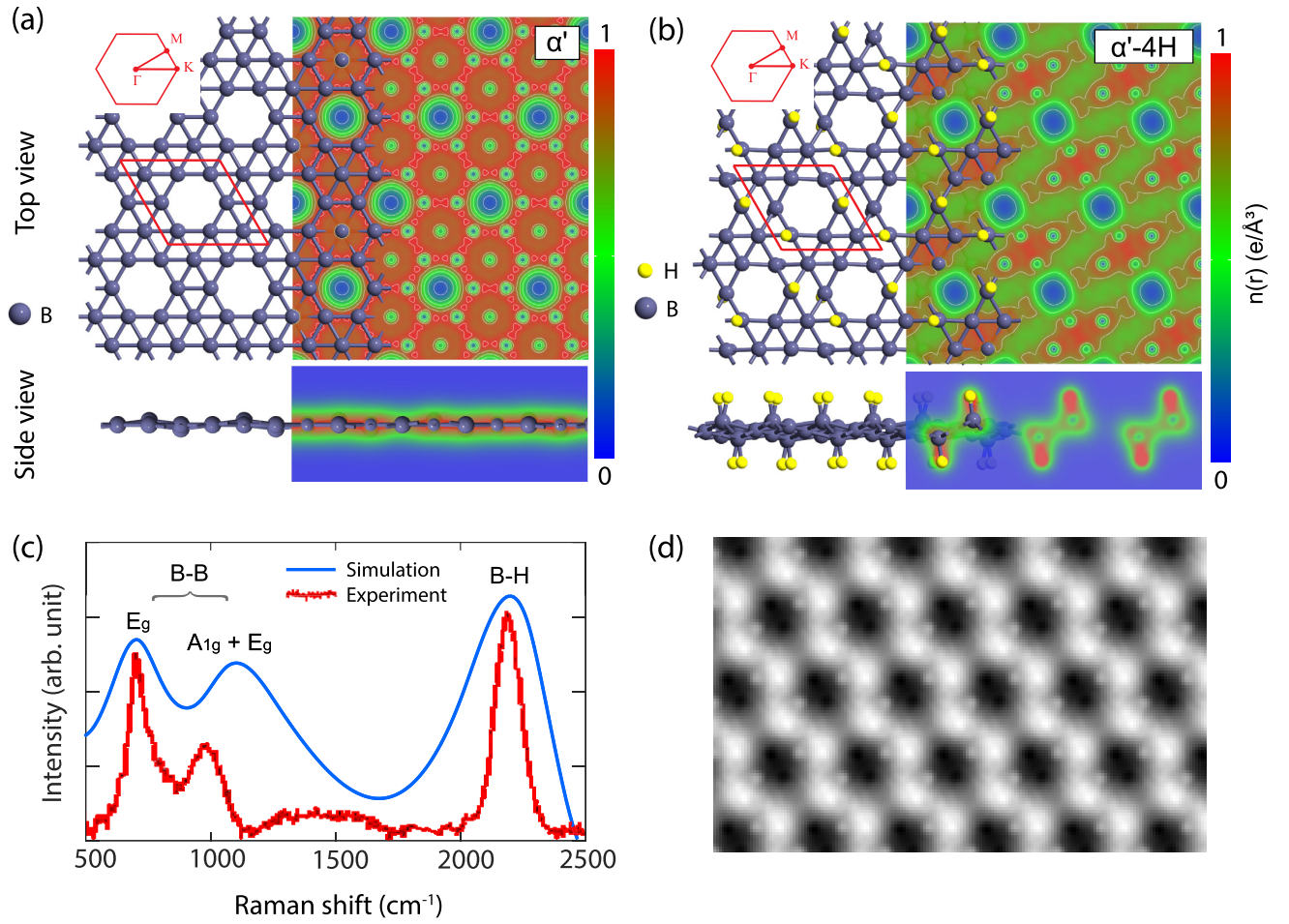


FIG. 1. [(a),(b)] Structural configurations and electron density cut planes of $\alpha'$ and $\alpha'$-4H borophenes. (c) Simulated Raman spectrum and (d) simulated STM image of $\alpha'$-4H borophene. The experimental spectra [12] was superposed on the simulated Raman spectrum for better comparison.

Figures 1(a) and 1(b) also indicate the electron density cut planes of $\alpha'$ and $\alpha'$-4H borophenes. In $\alpha'$ borophene, we can see a "sea of electrons", which is apparently the cause of its metallic nature. However, in $\alpha'$-4H borophene, an electron accumulation takes place around H atoms, which lowers the in-plane charge carrier distribution. This is in line with the Bader charge analysis, which confirms that 0.46 charge is transferred from B to H atoms.

As mentioned above, the $\alpha'$-4H borophene was synthesized recently [12]. To validate our model with the experiment, we performed simulations of Raman spectrum and scanning tunneling microscopy (STM). Figure 1(c) represents the Raman spectrum of $\alpha'$-4H borophene. We can see three peaks at about 710, 1100, and 2200 $cm^{-1}$, which are equivalent to 743, 1065, and 2500 $cm^{-1}$ observed in experiment [12]. The first two peaks are representatives of $E_g$ and $A_{1g} + E_g$ modes of the B-B cluster, and the last peak is associated with the combined modes of the B-H bonds. Also, Fig. 1(d) indicates the simulated STM image of $\alpha'$-4H borophene, which is very similar to the experimentally obtained images through HRTEM analysis [12].

Figure 2 summarizes the structural and electronic properties of $\alpha'$ and $\alpha'$-4H borophenes. As shown in the inset of Fig. 2(a), the atomic sites in$\alpha'$ borophene are classified into 6- and 5-bonded boron atoms, labeled with ⓐ and ⓑ, respectively. There are two ⓐ and six ⓑ sites in each unit cell and we can see both inversion and mirror symmetries. After hydrogenation, four B-B bonds in ⓑ sites are broken and replaced with four B-H bonds, which lead to novel sites labeled with ⓒ [see inset of Fig. 2(b)]. As a consequence, the mirror symmetry is broken in $\alpha'$-4H borophene. These structural modifications directly affect the electronic states and should be considered as the origin of different properties in the two borophenes.

Figure 2 also represents the partial density of states (PDOS) and orbital decomposed band structures of $\alpha'$ and $\alpha'$-4H borophenes at the GGA-PBE level. This information gives valuable insights into the contribution of each atomic site and orbital in the electronic properties. As it is clear from the PDOS, in $\alpha'$ borophene, $p_z$ orbitals of ⓑ sites are dominant. Given that $\alpha'$ borophene is almost flat, $p_z$ orbitals are perpendicular to neighboring $p_{x(y)}$ orbitals and no hybridization takes place between them. However, in $\alpha'$-4H borophene, as hydrogenation pulls some of boron atoms labeled with ⓒ out of the plane and forms a buckled structure, $p_z$ orbitals of ⓒ atoms are no longer perpen-

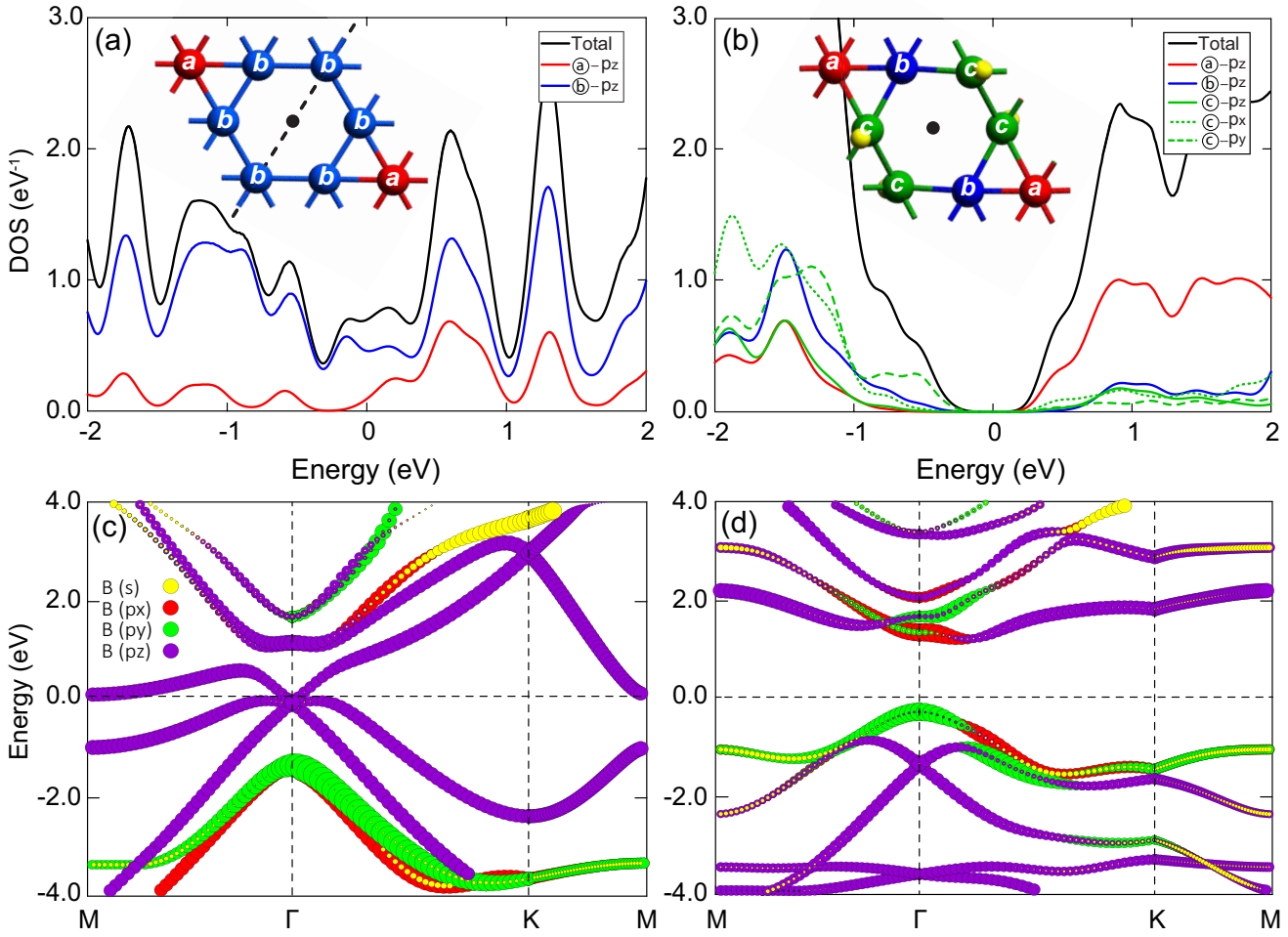


FIG. 2. [(a),(b)] Partial density of states (PDOS) of $\alpha'$ and $\alpha'$-4H borophenes, showing the significant contributing orbitals of the labeled atomic sites shown in the insets. Full results of PDOS are also available in Fig. S1 of the Supplemental Material [51]. [(c),(d)] Orbital decomposed band structures of $\alpha'$ and $\alpha'$-4H borophenes. Both PDOS and band structure were calculated at the GGA-PBE level.

dicular to neighboring $p_{x(y)}$ orbitals, which results in hybrid bonds.

The orbital hybridization can be seen from a different point of view through the orbital decomposed band structures. In $\alpha'$ borophene, we can see a triple energy degeneracy of pure $p_z$ orbitals. These triple Dirac fermions were previously observed in other flat borophenes in experimental and theoretical studies [53,54]. However, hydrogenation leads to a hybridization between atomic orbitals and diminishes this degeneracy. Subsequently, $\alpha'$-4H borophene finds dominated occupied ⓒ-$p_y$ states and unoccupied ⓐ-$p_z$ states in the valence and conduction band edges, respectively, which are separated with a relatively wide band gap.

These results are completely supported by the shapes of the wave functions of $\alpha'$-4H borophene at the VBM and CBM as shown in Fig. S2 of Supplemental Material [51]. At the VBM, the wave function is shaped like a dumbbell, which is distributed along the $y$-axis and centered on ⓒ atoms, showing the contribution of ⓒ-$p_y$ orbitals. At the CBM, the dumbbell-shaped wave function has components along both $x$ axis and $z$ axis, showing thehybridization between ⓒ-$p_x$ and ⓐ-$p_z$ orbitals.

To highlight the role of buckling and orbital hybridization in opening the band gap, we calculated the band structure for a conceptual model of flat $\alpha'$-4H borophene. We optimized $\alpha'$-4H borophene with a fixed $z$ component, to have the same buckling as $\alpha'$ borophene. The resulting band structure is available in Fig. S3 [51], showing no band gap. Therefore, we can conclude that the buckling induced by ⓒ atoms is a strong cause for opening the band gap. It should be noted that the role of buckling in opening energy band gap has been widely considered in the community [55–57].

The band gap calculated at the GGA-PBE level is 1.49 eV, which is underestimated by 1.0 eV compared to the experiment [12]. Using the HSE03 and HSE06 hybrid functionals and considering a fraction of the exact exchange, the band gap is corrected to be 1.85 and 1.98 eV, respectively (see Fig. S4 [51]). Eventually, at the PBE0 level, the band gap is found to be 2.54 eV, in excellent agreement with the experimental band gap measured by UV-V spectrum (2.49 eV).

From the band structure, it is also seen that the VBM is located at the Γ point and the CBM is located somewhere between the Γ and $K$ points. The valence and conduction band edges are parabolically dispersed, which indicate free charge

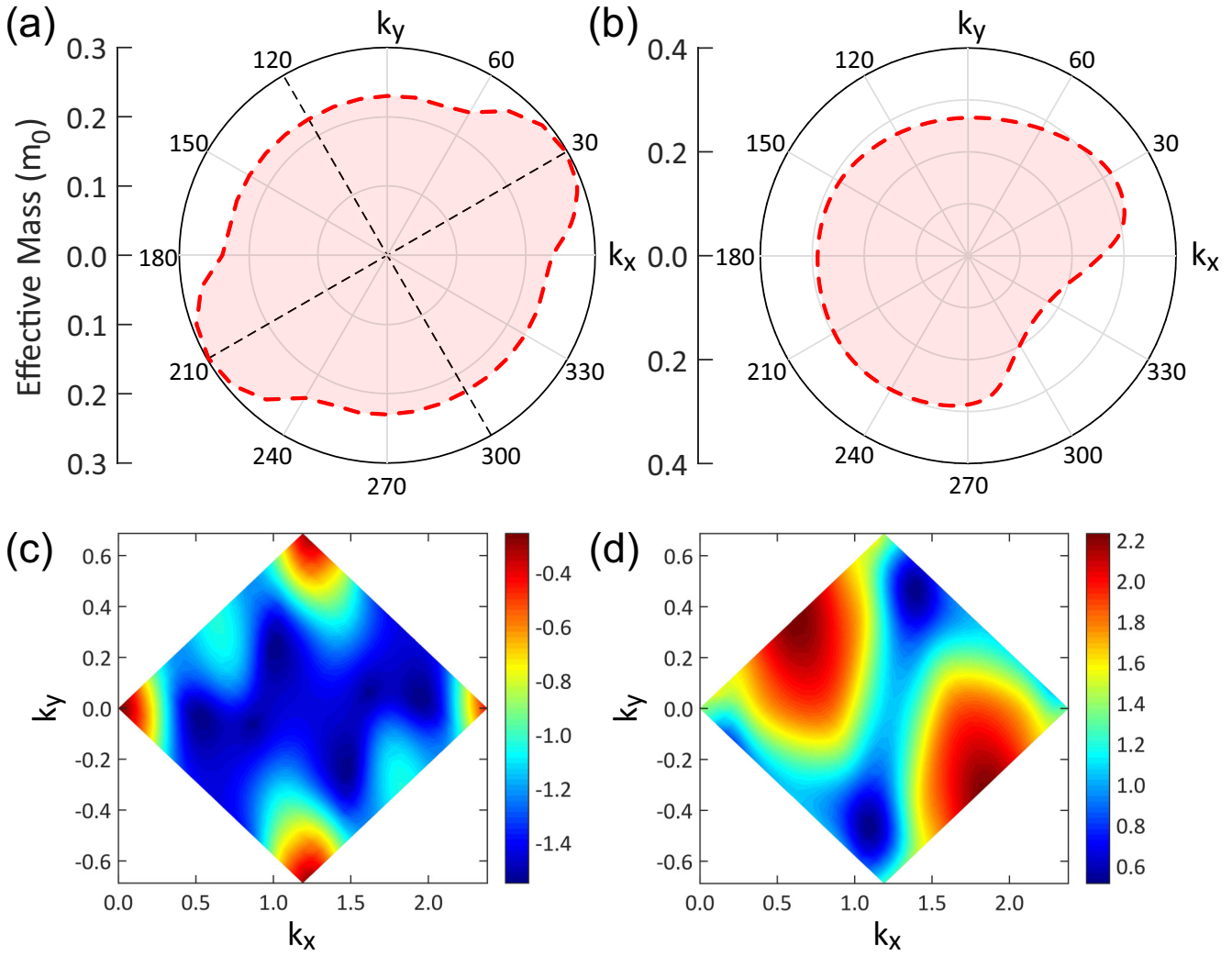


FIG. 3. Angular-dependent effective mass of $\alpha'$-4H borophene for (a) holes and (b) electrons together with 2D contour plot of (c) HOMO and (d) LUMO at the PBE level.

carriers. The effective mass of holes is estimated to be 0.23 and 0.24 $m_0$ for the VBM $\rightarrow$ M and VBM $\rightarrow$ K directions while the effective mass of electrons is predicted to be 0.30 and 0.23 $m_0$ for the CBM $\rightarrow$ $\Gamma$ and CBM $\rightarrow$ K directions, respectively.

To analyze the anisotropic band dispersions near the VBM and CBM, we provided the angular-dependent effective mass of holes and electrons. As shown in Figs. 3(a) and 3(b), one can find that the effective mass curves at band edges are highly anisotropic. For holes, the effective mass is however symmetric along the lines of 30°, 120°, 210°, and 300° while it reaches the maximum value of 0.30 $m_0$ at 30° and 210°. Importantly, the effective mass is 0.24 and 0.23 $m_0$ along the VBM-X and VBM-Y directions, respectively. For electrons, no symmetry can be found. The effective mass of electrons reaches the maximum (minimum) value of 0.32 (0.18) $m_0$ at 30° (330°) while it is 0.25 and 0.27 $m_0$ along the CBM-X and CBM-Y directions, respectively. These anisotropic properties can also be found from the 2D contour plot of HOMO and LUMO as shown in Figs. 3(c) and 3(d) and could be beneficial to the separation of electrons and holes, which is highly desired in the photovoltaic field.

Although DFT gives adequate qualitative information about the electronic and optical properties, it does not account for the electron-electron and electron-hole interactions, which have a crucial role in 2D materials. Therefore, further investigations are required to be performed using many-body perturbation calculations.

The QP band gap predicted by many-body GW theory is very sensitive to input parameters including the spin-orbit coupling (SOC), $k$-point sampling, vacuum space, number of virtual bands, energy cutoff, self-consistent iteration, and frequency grid points. Therefore, it is mandatory to converge the band gap. We initially checked the effects of the SOC. Due to the small atomic mass of boron, except a slight downward shift in the electronic states, no noticeable spin splitting was found in the energy levels, and the band gap remained almost constant ($\Delta E_g \simeq 0.001$ eV). Hence, owing to its excessive computational costs and negligible impacts, this interaction is excluded from the rest of the calculations.

Next, we performed a bunch of calculations to converge the QP band gap at the $G_0W_0$ level as a function of the (a) $k$-point sampling of Brillouin zone using 40 virtual bands and $L_z = 20$ Å; (b) vacuum space using 40 virtual bands and 5 × 5 × 1 $k$-point mesh; and (c) the number of virtual bands using $L_z = 20$ Å and 5 × 5 × 1 $k$-point mesh as illustrated in Fig. S6 [51]. We realized that a 9 × 9 × 1 $k$-point mesh is enough for a satisfactory convergence within ∼0.05 eV. Such a dense $k$-point mesh is indispensable for an accurate description of the optical gap and binding energy. Due to the long-range nature of screened Coulomb interaction, the vacuum space plays a crucial role in the determination of the QP band gap. Generally, it is imposed to be between 20 to 30 Å. To ensure convergence within ∼ 0.05 eV, we set the vacuum space to be 25 Å, which is the highest accuracy we could computationally afford. Our results also verified that at least 40 virtual bands are required for our many-body GW calculations. The band gap is essentially the same when 80 bands are included (see Fig. S6 [51]). Such rapid convergence with respect to the number of unoccupied bands is mainly attributed to the absence of strongly localized states characterized by flat bands. In our GW calculations, 96 frequency grid points were employed for the energy integration. This is because we checked the convergence of QP band gap as a function of frequency grid points using 40 virtual bands and 5 × 5 × 1 k-point mesh. The band gap difference for two calculations (with 96 and 144 grid points) is less than 0.01 eV. Hence, we set the frequency grid points to be 96. Such grid points were already reported to be enough for the energy integration in the range of $0 - 10$ eV [36,58]. Moreover, we tested the convergence of the QP band gap with respect to the number of iterations in partially self-consistent $G_iW_0$ and $G_iW_i$ as shown in Fig. S6 [51]. Obviously, four iterations are sufficient to reach the convergence threshold of ∼ 0.001 eV.

To ensure the accuracy of our many-body GW calculations, we calculated the QP band gaps of graphane (CH) and fluorographene (CF) monolayers. For example, for graphane, the band gap was predicted to be 5.62, 5.81, and 6.17 eV under the $G_0W_0$, $GW_0$, and GW levels of theory, respectively, which are in excellent agreement with 5.64, 5.89, and 6.28 eV reported in previous papers [36]. Also, the band gaps obtained for fluorographene agree very well with previous values as listed in Table S2 of the Supplemental Material [51].

After validation of the required accuracy, now we turn our attention to the GW results. The general shape of the QP band structure at the $G_0W_0$ level is similar to that obtained by the PBE functional as shown in Fig. S4 [51]. The inclusion of electron-electron interaction enlarges the band gap from 1.49 up to 1.98 eV. This value is larger than that of the HSE03 and exactly equals to that obtained by the HSE06. In other words, a similar accuracy is achieved by the $G_0W_0$ as by the HSE06. At the $GW_0$ and GW levels, the QP band gap increases up to 2.23 and 2.52 eV, making the self-energy correction to be 0.74 and 1.03 eV, respectively. Overall, one can say that the partially self-consistent GW offers an accuracy similar to the PBE0 functional and is in excellent agreement with the experiment [12]. Also, the direct QP band gap at the Γ point are 3.09, 3.31, and 3.58 eV for $G_0W_0$, $GW_0$, and GW levels, respectively. It is worth noting that owing to the separation of the QP energy states in the conduction band, just a rigid shift of the conduction band with respect to the valence band may not capture the self-energy effects properly. The same findings were reported for other 2D materials, where there is no simple "scissor rule" to obtain the QP band structure from that of the LDA/PBE [59,60].

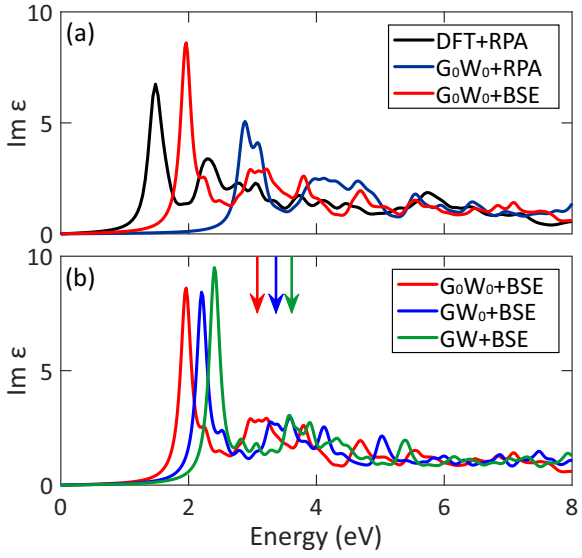


FIG. 4. (a) The imaginary part of the dielectric function of $\alpha'$-4H borophene for light polarized along the x-direction ($E \| x$) at different levels of theory: DFT+RPA (e-e and e-h correlations neglected), $G_0W_0$+RPA (e-e correlation included and e-h correlation neglected), and $G_0W_0$+BSE (both e-e and e-h correlations included). (b) The imaginary part of the dielectric function of $\alpha'$-4H borophene at different degrees of self-consistency in the GW. The direct QP band gaps are shown with arrows.

### B. Optical properties

Excitonic effects are significantly enhanced in 2D materials [61,62]. This is mainly due to the reduced Coulomb screening and geometrical confinement. These effects play a crucial role in the optical properties of such materials. Hence, to have a reliable description of the optical properties, it is indispensable to take the electron-hole Coulomb interaction into account. In this section, we aim to present the excitonic optical spectra of $\alpha'$-4H borophene achieved from solving the Bethe-Salpeter equation on top of various levels of the GW. To fully appreciate the many-body effects, we also calculated the optical spectra within the random-phase approximation (RPA) on top of the DFT and GW, where the electron-hole interaction is neglected. First, we checked the convergence of optical spectra $\alpha'$-4H borophene for some input parameters. More details are available in the Supplemental Material [51], Fig. S7 and Text S2.

Figure 4(a) exhibits the imaginary part of the macroscopic dielectric function for light polarized along the $x$ direction ($E \| x$) at different levels, namely DFT+RPA, $G_0W_0$+RPA, and $G_0W_0$+BSE. As can be seen, the inclusion of electron-electron correlation completely reshapes the optical spectrum and leads to a significant blueshift (∼1.4 eV), which is due to the self-energy correction. On the other hand, the electron-hole correlation results in a redshift (∼0.92 eV) in

the optical spectrum, owing to the cancellation effect between self-energy correction and excitonic effects. The electron-hole correlation also leads to an increase (decrease) in the oscillator strength of the first (second) peak. However, its main impact is the appearance of some bound excitons below the $G_0W_0$ direct band gap (3.09 eV) at the Γ point, which are missing in the $G_0W_0$+RPA spectrum.

The DFT+RPA predicts the absorption edge to be 1.48 eV, which is very close to the PBE band gap (1.49 eV). The first two peaks at $G_0W_0$+RPA appear at 2.88 and 3.08 eV, respectively. They are near the $G_0W_0$ direct band gap (3.09 eV) at the Γ point. Most importantly, the first peak at $G_0W_0$+BSE (∼ 1.96 eV) is found to lie between the PBE (1.49 eV) and $G_0W_0$ (1.98 eV) band gaps as it includes both the QP correction and excitonic effects. This peak (the so-called optical gap) originates from the direct transition (bright exciton) from the VBM to the conduction band, and corresponds to a strongly bound exciton with a binding energy of $E_b \simeq 1.13$ eV. It is worth mentioning that the exciton binding energy is determined by the difference between the QP direct band gap and optical gap. The optical gap obtained from $G_0W_0$+BSE is ∼ 0.53 eV smaller than the experimental gap achieved from photoluminescence measurement (2.49 eV) [12]. This underestimation is attributed to the overscreening effects associated with building the susceptibility based on an underestimated band gap. Indeed, the small Kohn-Sham band gap leads to a spurious enhancement of screening, and subsequently, to an underestimated optical gap.

For the considerable dependence of the $G_0W_0$ on the Kohn-Sham starting point and the exclusion of many-body exchange and correlation in the ground-state eigenvalues, we examined the effects of self-consistency. Figure 4(b) indicates the optical spectra of $\alpha'$-4H borophene for light polarized along the $x$ direction under different degrees of self-consistency in the GW. As can be seen, iteratively updating the QP eigenvalues in the Green's function results in a blueshift (∼ 0.24 eV) in the optical spectrum because it reduces the overestimation of the screening observed in the $G_0W_0$. At this level of theory (i.e., $GW_0$+BSE), the shape of the spectrum is relatively preserved, and the optical gap is estimated to be ∼ 2.20 eV with a binding energy of $E_b \simeq 1.11$ eV. Therefore, one can say that $E_b$ is independent of the self-consistency in Green's function. Moreover, the oscillator strength is only redistributed to higher energies with no considerable change compared to that of the $G_0W_0$+BSE level.

Updating the screened Coulomb potential leads to a blueshift (∼ 0.20 eV) as well, implying a larger self-energy correction in the GW compared to those in the $G_0W_0$ and $GW_0$. The highest level of theory (i.e., GW+BSE) predicts the optical gap to be ∼ 2.40 eV, which is slightly smaller than the GW band gap of ∼ 2.52 eV. This value agrees very well with the experimental gap (2.49 eV) [12] because GW+BSE incorporates many-body effects in the ground-state eigenvalues and meaningfully reduces the dependence on the DFT starting point using self-consistency. Here, the $E_b$ is obtained 1.18 eV, suggesting relatively stronger cancellation effects. Such a huge $E_b$ is a signature of a strongly bound exciton, showing ultrahigh stability of excitonic states against thermal dissociation, making $\alpha'$-4H borophene a very promising candidate for room-temperature optical applications. The final value is larger than those of phosphorene (0.86 eV), $MoS_2$ (0.96 eV), h-BN (0.80 eV), and many other semiconducting monolayers [63–66], turning $\alpha'$-4H borophene into a highly competitive candidate for optical applications. As the GW+BSE level offers the best description, its corresponding oscillator strength is shown in Fig. S8 [51].

It is worth mentioning that the QP band gap and exciton binding energy calculated at all three levels of theory (i.e., $G_0W_0$, $GW_0$, and GW) show an excellent agreement with the linear scaling law given as, $E_b = 0.21\,E_g + 0.40$ [58]. The standard deviations are less than 0.05 eV, which can indicate there points. First, our results have been converged very well. Second, the linear scaling law is independent of the level of accuracy. Third, it is also true for functionalized 2D materials. More importantly, we check if its true for strained $\alpha'$-4H borophene. For instance, under the strain of 4%, the $G_0W_0$ band gap and exciton binding energy are 2.4 and 0.8 eV, respectively, approving the broad applicability of this scaling law.

As shown above, the inclusion of excitonic effects have a significant impact on the dielectric function of $\alpha'$-4H borophene. Therefore, for the rest of our optical investigations, we concentrate on the GW+BSE level, which is expected to obtain the most reliable results. Moreover, as shown in Fig. S11 [51], because of the huge depolarization effect in 2D materials for the light polarization perpendicular to the surface [67], the optical spectrum for $E\|z$ polarization is negligible. Therefore, we only focus on the in-plane polarizations. Figure 5 shows the real and imaginary parts of the dielectric function as well as the optical absorption spectrum for the incident light polarized along the $x$ (E$\|x$) and $y$ (E$\|y$) directions. The spectra of extinction coefficient ($k$), electron energy loss ($L$), refraction index ($n$), and reflectance ($R$) are available in Fig. S12 [51]. We can see different fluctuations in optical spectra with different polarizations, as a consequence of the structural anisotropy. From the real part of the dielectric function, the static dielectric constant is found to be 3.0 and 2.6 for $E\|x$ and $E\|y$ polarizations, respectively. Moreover, we see a sign of metallic nature by negative values for $E\|x$ within the range of 2.36 to 2.52 eV (525 to 492 nm), which is absent for $E\|y$, where the real part is positive all over the spectrum. This is also approved by the reflectance spectrum which shows a nearly 40% reflectance for $E\|x$ within this area.

From the imaginary part, it is clear that, although the first peaks of the spectrum are uniquely at ∼2.20 eV for $E\|x$ and $E\|y$, which shows the same optical band gaps, the intensity of the peaks are higher for $E\|x$, indicating a stronger electron transition by $E\|x$ polarized light. This is also approved by the extinction coefficient and absorption spectrum, where the intensity of $E\|x$ first peak is more than two times equal to the $E\|y$ one. Such in-plane optical anisotropy provides an additional degree of freedom for optoelectronic devices.

Regardless of the polarization, the absorption edge ($\alpha > 10^6$ cm$^{-1}$) is around the edge of the visible light (photon energy > 1.63 eV), therefore we predict that, as a device, $\alpha'$-4H borophene has a good chance of not getting hot by infrared radiations. The maximum absorption of visible light at optical bang gap is 4.82 and $2.34\times10^7$ m$^{-1}$ for $E\|x$ and $E\|y$ polarizations, respectively. Moreover, the mean value of absorption within the visible area is 1.68 and $1.13 \times 10^7$ m$^{-1}$

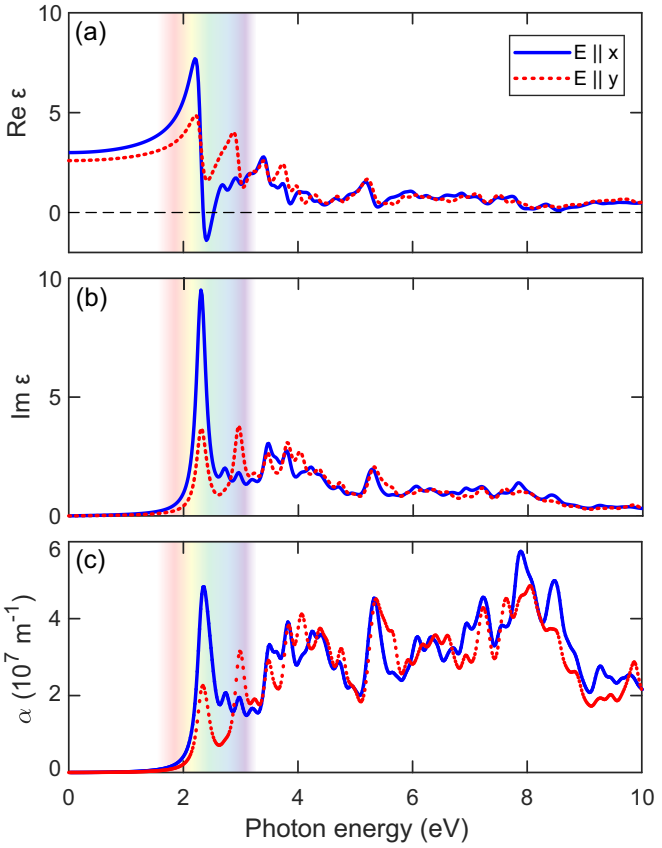


FIG. 5. Optical properties of $\alpha'$-4H borophene with incident light polarized along x and y directions at the GW+BSE level of theory. (a) Real and (b) imaginary parts of the dielectric function. (c) Optical absorption spectrum. For better assessment, the visible area is shown by a schematic color spectrum within 1.63 to 3.26 eV.

for $E\|x$ and $E\|y$ polarizations, which approves the linear dichroism for visible light. The absorption in ultraviolet region fluctuates increasingly, up to the maximum value of 5.74 and 4.86 for $E\|x$ and $E\|x$ in far ultraviolet around 8 eV. The static refractive index is calculated to be 1.73 (1.77) for $E\|x(E\|y)$ polarization. Other optical parameters are summarized in Table S3 of the Supplemental Material [51].

To demonstrate the contribution of interband transitions in optical absorption, we show the total and partial joint density of states (JDOS) of $\alpha'$-4H borophene in Fig. 6(a). The total JDOS includes all possible interband transitions from all the valence to all the conduction bands while the partial JDOS involves only the interband transitions from a specific valence band to a specific conduction band. As can be seen from the partial JDOS, the visible area is dominated by the transitions from the highest valence band to the lowest conduction band (i.e., V → C1) while a weak contribution is observed from other transitions. The total JDOS reveals a shoulder at 1.63 eV and a peak at 3.29 eV, which are associated with the direct transitions at the Γ and $K$ valleys, respectively. A few of forbidden (black arrows) and allowed (colored arrows) transitions are illustrated in Fig. 6(b). Also, Fig. 6(c) represents the probability of transitions between two states. As it is clear, the transition dipole moment amplitude is 184 and 486 Debye$^2$ for transitions V → C1 and V → C2 at the Γ point, respectively, while it is zero for transition V → C3 at this point, implying no optical absorption between these two states.

We additionally calculated the effective mass and Bohr radius of the ground-state exciton based on Eqs. (16) and (17). These formulas are generally used for Wannier exciton and might not be very accurate for Frenkel exciton. However, they are also employed to approximately estimate the effective mass and Bohr radius for Frenkel excitons [41,68]. At the GW+BSE level, the effective mass of exciton is 0.78 $m_0$, which refer to high localization. The Bohr radius of exciton

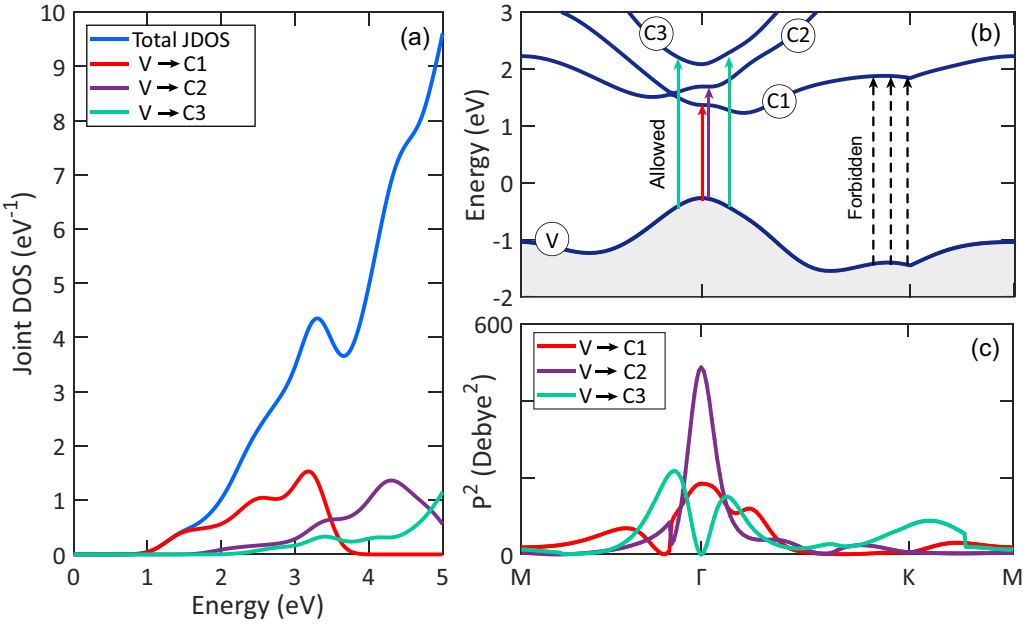


FIG. 6. (a) Total and partial joint DOS, (b) electronic band structure, and (c) transition dipole moment of $\alpha'$-4H borophene at the PBE level. The allowed dipole transitions are shown with colored arrows, while the forbidden transitions are depicted by dashed arrows.

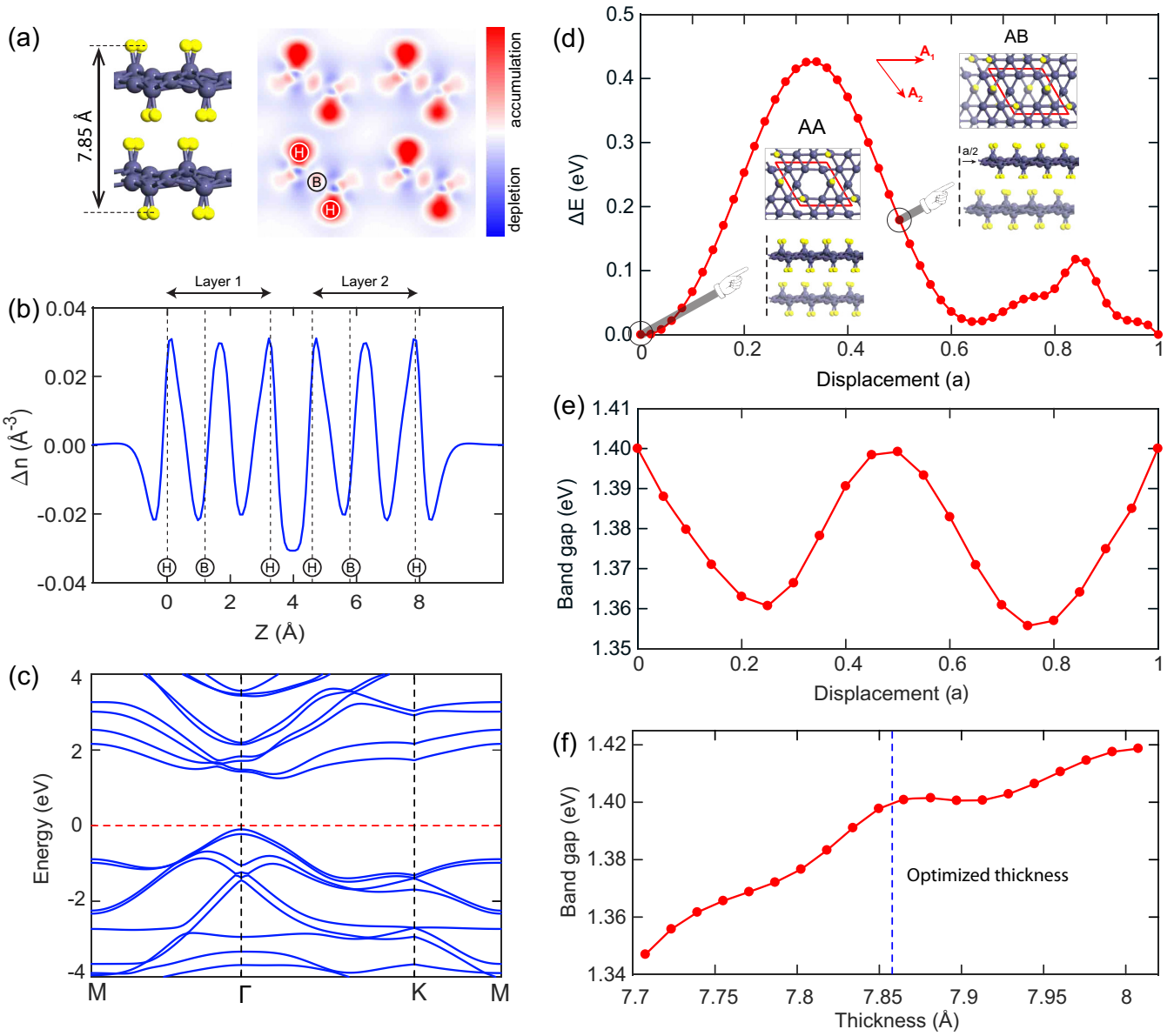


FIG. 7. Bilayer $\alpha'$-4H borophene. (a) Side view and electron difference density map. (b) Variation of electron difference density with buckling. (c) Band structure of AA stacking. (d) Variation of bilayer energy with displacement of the upper layer with respect to AA stacking. (e) Variation of bilayer band gap with displacement of the upper layer. (f) Variation of band gap of AA stacking with thickness.

is 2.03 Å, smaller than the lattice constant (5.05 Å). This value is smaller than that of $MoS_2$ (∼10 Å) monolayer [69], which means the electron and hole are restricted in a narrower area, therefore, they have stronger interaction. Due to the large exciton binding energy and small Bohr radius, one can deduce that the excitons in $\alpha'$-4H borophene have the characteristics of a Frenkel exciton.

In this part, we investigate the variation of band gap and exciton binding energy under biaxial tensile strain (tension). As can be seen from Fig. S10 [51], by increasing the tension up to 10%, the QP and optical band gaps decrease by 0.4 and 0.7 eV, respectively. This is attributed to the reduction of buckling height under tension. Also, by increasing the tension up to 10%, the exciton binding energy experiences a decrease of 0.3 eV, which means the excitonic states are robust against tension. These calculations were performed at the $G_0W_0$ level of theory but they are similar to the results at the higher levels (i.e., $GW_0$ and GW). It should be noted, in our previous paper [32], we have shown the dynamical stability of $\alpha'$-4H borophene under such tension by phonon dispersion, stress-strain, and energy-strain curves.

### C. Bilayer $\alpha'$-4H borophene

The results of atomic force microscopy (AFM) have shown that the average thickness of a typical synthesized $\alpha'$-4H borophene is about 0.78 nm [12], which is higher than the monolayer. To understand the effects of thickness on the electronic properties of $\alpha'$-4H borophene, we studied the bilayer of this material at the GGA-PBE level of theory. For this, we firstly measured the vertical distance between layers by means of variation of energy to thickness. As shown in Fig. 7(a),

the optimized thickness of a bilayer is 0.785 nm, which is in great agreement with that measured through AFM. After gaining the interlayer distance, we re-optimized the structure with AA stacking. The electron difference density given in Figs. 7(a) and 7(b) show that while a high electron extracting takes place by hydrogen atoms, the two layers do not trade much electrons within themselves, which implies the absence of strong covalent bonds and presence of weak van der Waals interactions. This might be due to the screening of H atoms among the boron layers. Because of the weak force between the layers, the lattice constant and bond lengths of the bilayer do not have a significant difference with the monolayer.

As shown in Fig. 7(c), the AA-stacked bilayer $\alpha'$-4H borophene is an indirect semiconductor with a band gap of 1.4 eV. Most 2D materials experience a topological band gap transition from their monolayer to bilayer or multilayer forms. For instance, from monolayer to bilayer, graphene opens a bang gap of zero to 0.25 eV [70] and, on the contrary, $\beta$ antimonene closes its band gapfrom 0.76 eV to zero [71]. However, for the weak van der Waals interaction in bilayer $\alpha'$-4H borophene, it experiences a very small gap change. The VBM is located at Γ point and the CBM is within the Γ-K path.

In the VBM and CBM, the band dispersion is parabolic, which exhibits high mobility of electrons and holes. This inclines the high potential of $\alpha'$-4H borophene in optoelectronic applications, even for thicknesses more than monolayer.

To see the impact of stacking mode on the electronic properties of bilayer, we slipped the upper layer along the lattice vector $\mathbf{A}_1$ as much as percentages of lattice constant ($a$). The energy difference between different stackings with respect to AA stacking is indicated in Fig. 7(d), which is less than 20 meV. These stackings can form Moiré patterns in borophene with no need to external strain or requirement of large superlattices. Our investigations show that stacking mode does not have significant impact on the band gap of borophene. Theband gap remains indirect in all the stackings and, as shown in Fig. 7(e), it fluctuate mildly around the band gap of the AA stacking. When the displacement changes as half of the lattice constant (AB stacking), the band gap becomes equal to the band gap of the AA stacking. Because different stackings do not have very different band gaps, it might be not possible to determine the stacking mode of bilayer $\alpha'$-4H borophene through absorption spectrum. Furthermore, the experiment had not shown different band gaps for any sample [12].

To understand the dependence of electronic properties on the vertical distance between the layers, variation of band gap with interlayer distance is shown in Fig. 7(f). Herein, with conserving the atomic arrangements, we tuned the interlayer distance to have thicknesses between 7.7 to 8 Å. We can see a mild increase of band gap with the increase of the thickness. In other words, a high increase in the distance cancels the weak van der Waals interaction between layers and renders the bilayer into two independent monolayers. On the contrary, decrease of vertical interlayer distance increases the interactions and leads to a mild decrease in the band gap. Our investigations show that interlayer distance does not have any impact on the nature of indirect band gap of $\alpha'$-4H borophene. It is suggested that for the weak van der Waals interaction between the layers and existence of light weight atoms, vertical pressure, and slipping of the layers might not cause significant change in the optical properties of the structure, therefore, no gap difference had been observed for different thicknesses in the experiment [12].

## V. CONCLUSIONS

In summary, we reported the electronic and excitonic optical properties of $\alpha'$-4H borophene using first-principles many-body calculations. We firstly demonstrated that hydrogenation increases the buckling height and breaks the mirror symmetry of $\alpha'$ borophene, which results in an orbital hybridization and opening of a wide band gap in $\alpha'$-4H borophene. We calculated the quasiparticle bang gap to be 1.98, 2.23, and 2.52 eV at the $G_0W_0$, $GW_0$, and GW levels of theory, respectively. In the following, we solved the Bethe-Salpeter equation on top of the GW to evaluate the optical properties. At GW+BSE level, the imaginary part of the dielectric function shows that the direct optical excitation is characterized by an optical band gap of ∼2.40 eV, which is in excellent agreement with the experiment (2.49 eV). The real part of the dielectric function has negative values for $E \| x$ polarization within the range of 2.36 to 2.52 eV, which is a sign of metallic nature for this polarization. The optical absorption shows a high linear dichroism within the visible area. The mean value of visible optical absorption was calculated to be 1.68 and 1.13 $\times 10^7$ $m^{-1}$ for $E \| x$ and $E \| y$ polarizations, respectively. The exciton binding energy was calculated to be $\sim$ 1.18 eV, which is a signature of a strongly bound exciton, suggesting ultrahigh stability of excitonic states against thermal dissociation. The effective mass and Bohr radius of the ground-state exciton were obtained 0.78 $m_0$ and 2.03 Å, respectively, which demonstrates the characteristics of Frenkel exciton. We also investigated the bilayer $\alpha'$-4H borophenes with different stackings and thicknesses. It was found that they have similar electronic properties to the monolayer, which gives them similar potentials. These features together with great air-stability and mechanical strength suggest $\alpha'$-4H borophene as a desirable material for flexible optoelectronic applications at room temperature.

## ACKNOWLEDGMENTS

We are thankful to the Research Council of the University of Guilan for the partial support of this research.

The authors declare that they have no conflict of interest.

[1] A. J. Mannix, Z. Zhang, N. P. Guisinger, B. I. Yakobson, and M. C. Hersam, Nat. Nanotechnol. **13**, 444 (2018).

[2] L. Liu, Z. Zhang, X. Liu, X. Xuan, B. I. Yakobson, M. C. Hersam, and W. Guo, Nano Lett. **20**, 1315 (2020).

[3] S. I. Vishkayi and M. B. Tagani, Nanomicro Lett. **10**, 14 (2018).
[4] S. I. Vishkayi and M. B. Tagani, Phys. Chem. Chem. Phys. **19**, 21461 (2017).
[5] S. I. Vishkayi and M. B. Tagani, Phys. Chem. Chem. Phys. **20**, 10493 (2018).
[6] A. J. Mannix, X.-F. Zhou, B. Kiraly, J. D. Wood, D. Alducin, B. D. Myers, X. Liu, B. L. Fisher, U. Santiago, and J. R. Guest, Science **350**, 1513 (2015).
[7] S. Saha, W. Linden, and L. Boeri, Phys. Rev. Materials **5**, L080601 (2021).
[8] A. Zavabeti, A. Jannat, L. Zhong, A. A. Haidry, Z. Yao, and J. Z. Ou, Nanomicro Lett. **12**, 66 (2020).
[9] S. Arabha, A. H. Akbarzadeh, and A. Rajabpour, Compos. B. Eng. **200**, 108260 (2020).
[10] D. Ayodhya and G. Veerabhadram, FlatChem **19**, 100150 (2020).
[11] I. Cabria, A. Lebon, M. Torres, L. Gallego, and A. Vega, Appl. Surf. Sci. **562**, 150019 (2021).
[12] C. Hou, G. Tai, J. Hao, L. Sheng, B. Liu, and Z. Wu, Angew. Chem. **132**, 10911 (2020).
[13] Z. Xie, X. Meng, X. Li, W. Liang, W. Huang, K. Chen, J. Chen, C. Xing, M. Qiu, B. Zhang *et al.*, Research **2020**, 2624617 (2020).
[14] C. D. Entwistle and T. B. Marder, Angew. Chem. Int. Ed. **41**, 2927 (2002).
[15] L. Kong, L. Liu, L. Chen, Q. Zhong, P. Cheng, H. Li, Z. Zhang, and K. Wu, Nanoscale **11**, 15605 (2019).
[16] N. Powar and R. Pandav, J. Chem. Rev. **1**, 271 (2019).
[17] G. Bhattacharyya, A. Mahata, I. Choudhuri, and B. Pathak, J. Phys. D **50**, 405103 (2017).
[18] S. Suehara, T. Aizawa, and T. Sasaki, Phys. Rev. B **81**, 085423 (2010).
[19] T. Aizawa, S. Suehara, and S. Otani, Phys. Rev. Materials **5**, 064004 (2021).
[20] R. Wu, I. K. Drozdov, S. Eltinge, P. Zahl, S. Ismail-Beigi, I. Božović, and A. Gozar, Nat. Nanotechnol. **14**, 44 (2019).
[21] B. Kiraly, X. Liu, L. Wang, Z. Zhang, A. J. Mannix, B. L. Fisher, B. I. Yakobson, M. C. Hersam, and N. P. Guisinger, ACS Nano **13**, 3816 (2019).
[22] Q. Zhong, L. Kong, J. Gou, W. Li, S. Sheng, S. Yang, P. Cheng, H. Li, K. Wu, and L. Chen, Phys. Rev. Materials **1**, 021001(R) (2017).
[23] H. Liu, J. Gao, and J. Zhao, Sci. Rep. **3**, 3238 (2013).
[24] C. R. Ryder, J. D. Wood, S. A. Wells, Y. Yang, D. Jariwala, T. J. Marks, G. C. Schatz, and M. C. Hersam, Nat. Chem. **8**, 597 (2016).
[25] A. Kochaev, R. Meftakhutdinov, R. Sibatov, K. Katin, M. Maslov, and V. Efimov, Appl. Surf. Sci. **562**, 150150 (2021).
[26] B. A. Baraiya, N. N. Som, V. Mankad, G. Wu, J. Wang, and P. K. Jha, Appl. Surf. Sci. **527**, 146852 (2020).
[27] Q. Li, V. S. C. Kolluru, M. S. Rahn, E. Schwenker, S. Li, R. G. Hennig, P. Darancet, M. K. Y. Chan, and M. C. Hersam, Science **371**, 1143 (2021).
[28] M. A. Mohebpour, S. M. Mozvashi, S. I. Vishkayi, and M. B. Tagani, Sci. Rep. **10**, 14963 (2020).
[29] I. Tateishi, N. T. Cuong, C. A. S. Moura, M. Cameau, R. Ishibiki, A. Fujino, S. Okada, A. Yamamoto, M. Araki, S. Ito, S. Yamamoto, M. Niibe, T. Tokushima, D. E. Weibel, T. Kondo, M. Ogata, and I. Matsuda, Phys. Rev. Materials **3**, 024004 (2019).
[30] G. R. Schleder, E. Marinho Jr, D. J. R. Baquiao, Y. M. Celaschi, F. Gollino, G. M. Dalpian, and P. A. S. Autreto, Phys. Rev. Materials **4**, 074005 (2020).
[31] X. Wu, J. Dai, Y. Zhao, Z. Zhuo, J. Yang, and X. C. Zeng, ACS Nano **6**, 7443 (2012).
[32] S. M. Mozvashi, M. A. Mohebpour, S. I. Vishkayi, and M. B. Tagani, Sci. Rep. **11**, 7547 (2021).
[33] M. Shishkin and G. Kresse, Phys. Rev. B **75**, 235102 (2007).
[34] M. S. Hybertsen and S. G. Louie, Phys. Rev. B **34**, 5390 (1986).
[35] C. Liu, J. Kloppenburg, Y. Yao, X. Ren, H. Appel, Y. Kanai, and V. Blum, J. Chem. Phys. **152**, 044105 (2020).
[36] F. Karlicky and M. Otyepka, J. Chem. Theory Comput. **9**, 4155 (2013).
[37] M. Shahrokhi and C. Leonard, J. Alloys Compd. **682**, 254 (2016).
[38] M. Shishkin and G. Kresse, Phys. Rev. B **74**, 035101 (2006).
[39] X. Blase, I. Duchemin, D. Jacquemin, and P.-F. Loos, J. Phys. Chem. Lett. **11**, 7371 (2020).
[40] M. Gajdoš, K. Hummer, G. Kresse, J. Furthmüller, and F. Bechstedt, Phys. Rev. B **73**, 045112 (2006).
[41] M. Shahrokhi and C. Leonard, J. Alloys Compd. **693**, 1185 (2017).
[42] M. Rohlfing and S. G. Louie, Phys. Rev. Lett. **80**, 3320 (1998).
[43] M. Rohlfing and S. G. Louie, Phys. Rev. B **62**, 4927 (2000).
[44] C. Godet and M. Berberan-Santos, Diam. Relat. Mater. **10**, 168 (2001).
[45] P. Giannozzi, S. Baroni, N. Bonini, M. Calandra, R. Car, C. Cavazzoni, D. Ceresoli, G. L. Chiarotti, M. Cococcioni, and I. Dabo, J. Phys.: Condens. Matter **21**, 395502 (2009).
[46] B. Arnaud and M. Alouani, Phys. Rev. B **63**, 085208 (2001).
[47] G. Henkelman, A. Arnaldsson, and H. Jónsson, Comput. Mater. Sci. **36**, 354 (2006).
[48] M. Lazzeri and F. Mauri, Phys. Rev. Lett. **90**, 036401 (2003).
[49] J. Tersoff and D. R. Hamann, Phys. Rev. B **31**, 805 (1985).
[50] K. Choudhary, K. F. Garrity, C. Camp, S. V. Kalinin, R. Vasudevan, M. Ziatdinov, and F. Tavazza, Sci. Data **8**, 57 (2021).
[51] See Supplemental Material at http://link.aps.org/supplemental/10.1103/PhysRevMaterials.6.014012 for more details on the theoretical formulations and physical properties of the material.
[52] A. A. Mostofi, J. R. Yates, G. Pizzi, Y.-S. Lee, I. Souza, D. Vanderbilt, and N. Marzari, Comput. Phys. Commun. **185**, 2309 (2014).
[53] M. Ezawa, Phys. Rev. B **96**, 035425 (2017).
[54] B. Feng, O. Sugino, R. Y. Liu, J. Zhang, R. Yukawa, M. Kawamura, T. Iimori, H. Kim, Y. Hasegawa, H. Li, L. Chen, K. Wu, H. Kumigashira, F. Komori, T. C. Chiang, S. Meng, and I. Matsuda, Phys. Rev. Lett. **118**, 096401 (2017).
[55] S. K. Radha and W. R. L. Lambrecht, Phys. Rev. B **101**, 235111 (2020).
[56] Y. Umeno, M. Sato, M. Sato, and H. Shima, Phys. Rev. B **100**, 155116 (2019).
[57] A. Nijamudheen, R. Bhattacharjee, S. Choudhury, and A. Datta, J. Phys. Chem. C **119**, 3802 (2015).
[58] J.-H. Choi, P. Cui, H. Lan, and Z. Zhang, Phys. Rev. Lett. **115**, 066403 (2015).
[59] G. Luo, X. Qian, H. Liu, R. Qin, J. Zhou, L. Li, Z. Gao, E. Wang, W.-N. Mei, J. Lu, Y. Li, and S. Nagase, Phys. Rev. B **84**, 075439 (2011).

[60] S. Piccinin, Phys. Chem. Chem. Phys. **21**, 2957 (2019).
[61] P. Cudazzo, C. Attacalite, I. V. Tokatly, and A. Rubio, Phys. Rev. Lett. **104**, 226804 (2010).
[62] L. Yang, J. Deslippe, C.-H. Park, M. L. Cohen, and S. G. Louie, Phys. Rev. Lett. **103**, 186802 (2009).
[63] D. Y. Qiu, F. H. da Jornada, and S. G. Louie, Phys. Rev. Lett. **111**, 216805 (2013).
[64] M. Kolos and F. Karlický, Phys. Chem. Chem. Phys. **21**, 3999 (2019).
[65] L. Xu, M. Yang, S. J. Wang, and Y. P. Feng, Phys. Rev. B **95**, 235434 (2017).
[66] V. Tran, R. Soklaski, Y. Liang, and L. Yang, Phys. Rev. B **89**, 235319 (2014).
[67] L. Yang, C. D. Spataru, S. G. Louie, and M.-Y. Chou, Phys. Rev. B **75**, 201304(R) (2007).
[68] M. Shahrokhi, Appl. Surf. Sci. **390**, 377 (2016).
[69] T. C. Berkelbach, M. S. Hybertsen, and D. R. Reichman, Phys. Rev. B **88**, 045318 (2013).
[70] Y. Zhang, T.-T. Tang, C. Girit, Z. Hao, M. C. Martin, A. Zettl, M. F. Crommie, Y. R. Shen, and F. Wang, Nature (London) **459**, 820 (2009).
[71] G. Wang, R. Pandey, and S. P. Karna, ACS Appl. Mater. Interfaces **7**, 11490 (2015).